ACS APPLIED MATERIALS & INTERFACES

RESEARCH ARTICLE

www.acsami.org

Patterning of Red, Green, and Blue Luminescent Films Based on $CaWO_4:Eu^{3+}$, $CaWO_4:Tb^{3+}$, and $CaWO_4$ Phosphors via Microcontact Printing Route

Wenxin Wang, Piaoping Yang, Ziyong Cheng,* Zhiyao Hou, Chunxia Li, and Jun Lin*

State Key Laboratory of Rare Earth Resource Utilization, Changchun Institute of Applied Chemistry, Chinese Academy of Sciences, Changchun 130022, P. R. China

ABSTRACT: The multicolor patterned luminescent films of $CaWO_4:Eu^{3+}$ (red), $CaWO_4:Tb^{3+}$ (green), and pure $CaWO_4$ (blue) on quartz substrates were fabricated by the facile and low-cost microcontact printing (μCP) method combining with the Pechini sol−gel route. On the basis of the μCP process, a hydrophobic self-assembled monolayer (SAM) was first created on the hydrophilic surface of quartz substrates by poly(dimethylsiloxane) (PDMS) mold printing, and then, the multicolor patterned luminescent films were selectively deposited on the hydrophilic regions via a spin coating process and heating treatment. The X-ray diffraction, optical microscopy, scanning electron microscopy, and photoluminescence (PL) spectra were used to characterize the structure and fluorescence properties of the corresponding samples. The results demonstrate that the μCP process can be used for patterning the inorganic phosphor materials and have potential for fabricating rare-earth luminescent pixels for the applications of display devices.

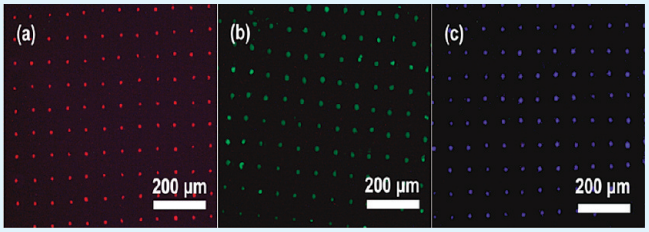

KEYWORDS: microcontact printing, patterning, $CaWO_4$, rare earth, luminescence

1. INTRODUCTION

A facile and rapid fabricating pattern structure with various features in micro- or nanoscale level is of great importance as a challenge for current scientific and technological researchers. Functional patterns with luminescent, magnetic, and electric properties become more attractive as the feature size of patterns are controlled in the nanoscale level because it means the higher resolution and more complicated microstructure can be established within the same area. For example, when the pattern array is used as sensor, the sensitivity to detect target molecules has a great increase with a higher resolution. Besides, the luminescent pattern arrays with different resolutions have been widely used as display devices in the range from television and computer panel to cell phone. The high-resolution phosphor patterning attracts great attention, owing to the current display requirements.[1−3] In general, high resolution display devices provide richer picture quality and bigger image size which improves the visual enjoyment. The realization of a full-color display device needs to deposit three primary color pixels (typically red, green, and blue) within a regular matrix. The patterning of the multicolor pixels arrays is of paramount importance for producing high-quality color images. The conventional patterning methods such as screen printing, vacuum deposition, and electro-deposition are generally based on the photolithography process which needs complicated layouts and expensive equipment.[4−6] Therefore, the realization of a highly ordered surface pattern with a process of flexibility, high throughput, low cost, and high controllability is still attractive. Recently, soft lithography techniques have attracted substantial interest as a pathway in the fabrication of surface microstructures.[7] The majority of these soft lithography techniques utilize a polydimethylsiloxane (PDMS) mold to print highly ordered micro- or nanopatterns. Among them, the microcontact printing (μCP) technique is most extensively investigated. In the μCP process, generally, the substrate surface is prepatterned with self-assemble monolayers (SAMs) and creates chemical heterogeneity on the surface. Therefore, some functional materials can be selectively grown or deposited on the desired regions.[8] In addition, the use of soft PDMS instead of rigid stamp in such type of printing method provides the opportunity to print patterns not only on flat but also on curved geometric substrates.[9] The PDMS stamp is prepared by casting prepolymer and the corresponding curing agent on a rigid mold with relief structure. After curing of the prepolymer, the PDMS exactly replicates the surface feature from the rigid mold. Therefore, the complicated pattern arrays of the rigid mold can be transferred to substrates by the flexible PDMS stamps with a great fidelity, and simultaneously, the PDMS stamps can be used repeatedly. Furthermore, solid state PDMS possess a very low interfacial free energy, which leads to a poor adhesion between the PDMS stamp surface and the attachments, allowing complete release of attachments from the stamp.

Rare-earth based luminescent materials have been widely used in display devices, lighting, optoelectronics technology, and bioassays.[10−12] Due to the abundant transitions within 4f−4f and

Received: June 21, 2011
Accepted: September 13, 2011
Published: September 13, 2011

dx.doi.org/10.1021/am2008008 | ACS Appl. Mater. Interfaces 2011, 3, 3921–3928

5d−4f configurations of rare earth ions, the multiple emission colors in the range from ultraviolet (UV) to visible to infrared (IR) light regions can be realized by changing host or doping with different rare earth ions.[13,14] Moreover, particle size and morphology of the materials also have effects on their luminescent properties. Rare earth based luminescent materials are generally prepared by the processes of solid state reaction, hydrothermal, solvent-thermal, coprecipitation, spray pyrolysis, sol−gel, and so on.[15,16] Among them, the Pechini-type sol−gel process is a facile and low-cost method for fabricating rare earth phosphors and their corresponding luminescent thin films.[17,18] This process generally employs the inorganic salts as precursors, citric acid as a chelate ligand, and poly (ethylene glycol) (PEG) as a cross-liking agent. In the Pechini sol−gel process, the viscosity of the precursor solution can be tuned by varying the content and/or molecular weight of the polymer and also the processing temperature to meet the requirements for film preparation.

Due to the attracting luminescent properties, metal tungstates have received much intensive investigation and have been applied in various fields such as X-ray intensified screen, scintillator materials, fluorescent lamps, and so on.[19]Among them, calcium tungstate ($CaWO_4$) is a self-activated blue-emitting luminescence material, and its luminescence properties could be altered by doping with rare earth ions. $CaWO_4$ based phosphors can be efficiently excited by short-wavelength ultraviolet radiation, X-rays, cathode rays, etc. Therefore, they have potential to be used as the functional phosphors in the display devices. In this paper, we reported the fabrication of red (R), green (G), and blue (B) luminescent pattern arrays based on the $CaWO_4$ (B) and Eu^{3+} (R) and Tb^{3+}(G)-doped $CaWO_4$ via the Pechini sol−gel process in combination with the microcontact printing technique. The pattern printing and phosphor synthesis process can be achieved within one step to reduce the cost of the production. The final RGB patterns of $CaWO_4$:Eu^{3+}, $CaWO_4$:Tb^{3+}, and pure $CaWO_4$ film arrays prepared by μCP method were clearly revealed by optical microscope. The photoluminescence (PL) spectra, lifetimes, and CIE coordinates were employed to characterize the fluorescence property of corresponding samples. The results demonstrate that the Pechini sol−gel process has good compatibility with soft lithography techniques for patterning the inorganic phosphor materials, which have potential for fabricating optical display devices.

2. EXPERIMENTAL SECTION

Materials. Rare earth oxides Eu_2O_3 (99.99%) and Tb_4O_7 (99.99%) were purchased from Science and Technology Parent Company of Changchun Institute of Applied Chemistry, and ammonium tungstate hydrate ($H_{26}N_6O_{41}W_{12}\cdot 18H_2O$) was purchased from Fluka. Calcium nitrate ($Ca(NO_3)_2\cdot 4H_2O$), citric acid, poly(ethylene glycol) (PEG), ethanol, *n*-octane, and nitric acid were purchased from Beijing Chemical Company. The prepolymer (Sylgard 184) and its curing agent for preparing poly(dimethylsiloxane) (PDMS) mold were purchased from Dow Corning Cooperation. All chemicals were analytical grade reagents without further purification. $Eu(NO_3)_3$ and $Tb(NO_3)_3$ solutions were prepared by dissolving corresponding rare earth oxides in nitric acid with heating to eject the superfluous HNO_3.

Here, we use $CaWO_4$:Eu^{3+} as a representative example to elucidate the experimental process. The Eu^{3+} ion doping concentration was 10 mol % of Ca^{2+} in the $CaWO_4$ host. First, 0.1 mmol of $Eu(NO_3)_3$, 0.9 mmol of $Ca(NO_3)_2\cdot 4H_2O$, and 0.275 g of $H_{26}N_6O_{41}W_{12}\cdot 18H_2O$ (1 mmol) were dissolved in 5 mL of deionized water, and the pH of the solution was kept between two and three by adding HNO_3. Then, the above solution was mixed with ethanol at the volume ratio of 1:2. The water−ethanol solution contains citric acid as the chelating agent for the metal ions, and the molar ratio of metal ions to citric acid was 1:2. A certain amount of PEG (0.2 g/mL, molecular weight = 20 000, A.R.) was added as a cross-linking agent to increase the solution viscosity. The precursor solution was stirred for 1 h to form a transparent sol solution, and the as-prepared solution was used as ink for the following soft lithography processes. The $CaWO_4$:Tb^{3+} precursor solution was prepared similarly with Tb^{3+} ion doping concentration of 5 mol % of Ca^{2+} in $CaWO_4$ using $Tb(NO_3)_3$ instead of $Eu(NO_3)_3$ in the above experimental process.

Scheme 1. Schematic Diagram of Experimental Process for Patterning $CaWO_4$:Eu^{3+} via the Microcontact Printing (μCP) Method[a]

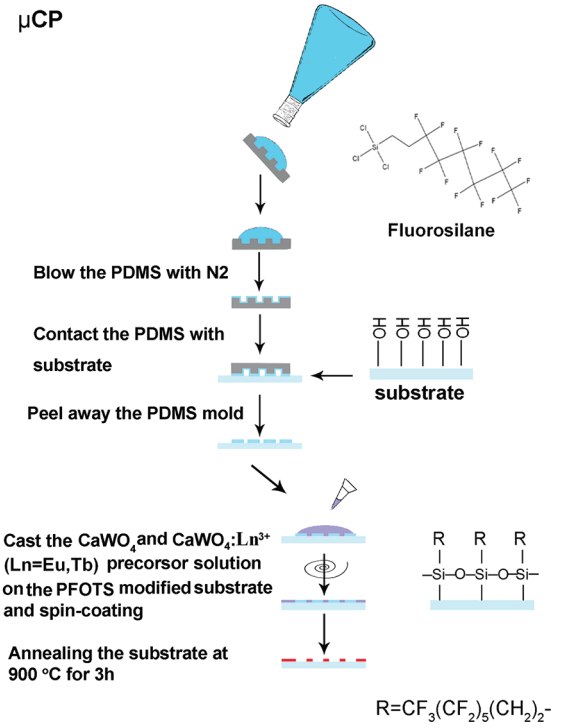

[a] The inset is the image of the PDMS stamp used in this technique.

The PDMS stamps were fabricated by casting PDMS prepolymer, a 10:1 (v/v) mixture of Sylgard silicone elastomer 184 and its curing agent, over a relief master prepared by photolithography. The elastomer was degassed for 30 min at room temperature and cured at 65 °C for 4 h, then peeled gently from the master. In this way, the PDMS stamps with a microwells shape were obtained.

Quartz plates were cleaned by immersing in a piranha solution of concentrated sulfuric acid and hydrogen peroxide (30%) with the volume ratio of 7:3 at 90 °C for 30 min, then rinsed with deionized water, and dried with nitrogen. The as-prepared quartz substrates exhibit hydrophilic property due to the hydroxyl group on the substrate surface. Caution: Piranha solution of peroxysulfuric acid is highly corrosive and potentially explosive, and it should be handled with great care.

μCP Process. The fabrication process of $CaWO_4$ and $CaWO_4$:Ln^{3+} (Ln = Eu, Tb) dot arrays via μCP is shown in Scheme 1. This technique is based on the modification of substrate surface and the selective deposition on the desire regions. Generally, the PDMS mold was flooded with the 1H,1H,2H,2H-perfluorooctyltrichlorosilane (PFOTS) solution in *n*-octane (1 vol %) and blew dry with N_2; then, the PDMS mold was placed in contact with the as-cleaned quartz substrate to print the self-assembled PFOTS monolayer (SAM). Next, the patterned substrate was

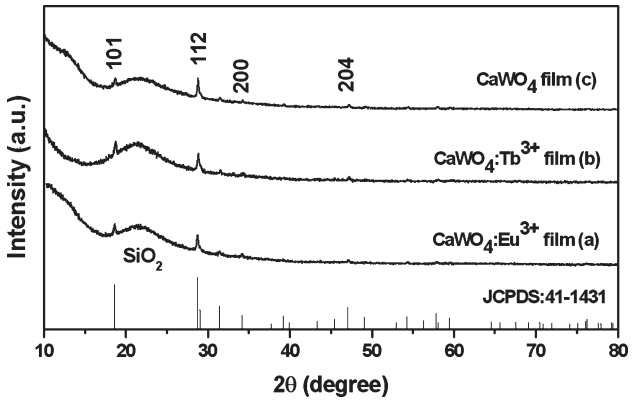

Figure 1. XRD patterns of calcined $CaWO_4:Eu^{3+}$ (a), $CaWO_4:Tb^{3+}$ (b), and $CaWO_4$ (c) film arrays fabricated by the microcontact printing method. The bottom of the figure shows the standard data for $CaWO_4$ (JCPDS Card 41-1431).

used as a template for the selective deposition of the metal salts solution by the spin-coating process. During the spin-coating process, the precursor solution was selectively deposited on the hydrophilic regions because of the poor adhesion between the solution and the SAM. Finally, the substrate with pattern gel was calcined at 900 °C for 3 h to obtain the final patterned crystalline $CaWO_4$, $CaWO_4:Eu^{3+}$, and $CaWO_4:Tb^{3+}$ films.

Characterization. The phase structures of the patterned $CaWO_4$, $CaWO_4:Eu^{3+}$, and $CaWO_4:Tb^{3+}$ film samples were characterized by X-ray diffraction (XRD) performed on a Bruk diffractometer with Cu Kα radiation (λ = 0.15405 nm). The patterned images were taken on an optical microscope by Leica THMSE600 attached with a digital CCD camera. Contact angles were measured via the system of Krüss DSA10-MK2, Germany, and the UV excitation luminescent micrographs were obtained by an inverted microscope (Nikon ECLIPSE TE2000) with a UV irradiation at 254 nm. The morphology of the samples was characterized by scanning electron microscope (SEM; S-4800, Hitachi). The photoluminescence (PL) excitation and emission spectra were performed on a Hitachi F-7000 spectrophotometer equipped with a 150w xenon lamp as the excitation source. The luminescence decay curves were obtained using a Lecroy Wave Runner 6100 digital oscilloscope (1 GHz) using a tunable laser (pulse width = 4 ns, gate = 50 ns) as excitation source (Continuum Sunlite OPO). All the measurements were performed at room temperature (RT).

3. RESULTS AND DISCUSSION

The methods we used to fabricate the RGB patterns arrays are given in the Experimental Section in detail. Scheme 1 illustrates the processes for fabricating pattern arrays by microcontact printing (μCP). The structures for the patterned thin films fabricated by the microcontact printing process were first examined by XRD. The XRD profiles of the patterned $CaWO_4:Eu^{3+}$, $CaWO_4:Tb^{3+}$, and pure $CaWO_4$ film annealed at 900 °C, together with the standard XRD data of $CaWO_4$, are shown in Figure 1. In the Figure 1a−c, there exists a broad peak centered at $2\theta = 22°$ due to amorphous SiO_2 of quartz plate and two relative strong and sharp peaks at $2\theta = 18.6°$ (101) and 28.7° (112) and some weak peaks at 34.2° (200) and 47.1° (204), respectively. They can be indexed to the tetragonal phase of $CaWO_4$ according to the standard $CaWO_4$ data (JCPDS Card 41-1431). No more reflections due to $CaWO_4$ and additional peaks for other phases have been found, because the patterned RGB pattern arrays are discontinuous and there exists blank regions under the light spot of X-ray, which greatly decrease the diffraction intensity. Additionally, the diffraction intensity of thin film is not comparable with the corresponding powder sample, because of the very small content of phosphors on substrates.[20]

Figure 2 shows the optical micrographs of $CaWO_4:Eu^{3+}$, $CaWO_4:Tb^{3+}$, and $CaWO_4$ patterned films before and after annealing, and the inset images are the SEM micrographs corresponding to the crystalline $CaWO_4:Ln^{3+}$ arrays. Figure 2a is the optical microscopy image of $CaWO_4:Eu^{3+}$ precursor gel pattern (just spin-coating dried, without annealing) fabricated by the patterning of hydrophobic SAMs via μCP technique first and then spin coating the precrusor solution of $CaWO_4:Eu^{3+}$ on the substrate. It can be seen that the ordered precursor gel arrays formed according to the pattern of PDMS stamp. The estimated diameter of the dots is 10.23 μm. After calcination at 900 °C in air, the patterned $CaWO_4:Eu^{3+}$ crystalline film was formed on the quartz plate and the corresponding optical image is shown in Figure 2d. The dots array corresponds to the final crystalline $CaWO_4:Eu^{3+}$, and the other region is the bare substrate after annealing. A size shrinkage of the dot gels was observed after annealing, owing to the pyrolysis and evaporation of the organic compounds in the gel. The edges of the dots were not as clear as that of the gel form because of the shrinkage after the heat treatment at 900 °C. The average diameter of the $CaWO_4:Eu^{3+}$ dots is 9.27 μm. The inset in Figure 2d is a scanning electron microscopy (SEM) image taken in the region of the $CaWO_4:Eu^{3+}$ phosphor dot, which indicates that the crystalline $CaWO_4:Eu^{3+}$ patterns are composed of nanoparticles with relative uniform size around 80 nm. The morphology of the dot patterns created via the μCP process remains unchanged before and after calcinations except that the size of the dots has slightly decreased with heat treatment. Similar to the above situation, the Figure 2b,e in the middle and Figure 2c,f at the bottom are the optical microscope images of the precursor pattern arrays and final crystalline patterns for $CaWO_4:Tb^{3+}$ and $CaWO_4$, respectively, and their inset images show the corresponding crystal grains of the phosphors under SEM observation. It can be seen that the film is uniform, without the big crack after calcining at high temperature, and mainly composed with the closely packed fine particles from 50 to 200 nm (measured in long axis). As shown in the insets of Figure 2d,e,f, the morphologies of the crystalline grains of $CaWO_4:Ln^{3+}$ phosphors display a slight difference, although they are fabricated under the identical condition. This may be caused by the doping (or undoping) of the different rare earth ions and their amounts in the phosphors. Generally, the morphologies of the crystalline grains have no obvious effect on the positions and shapes of the emission spectra in this situation because the emissions of Eu^{3+} and Tb^{3+} arise from f−f transtions which are strongly shielded by the outside 5s and 5p electrons. However, the PL intensities will have a slight difference due to the surface defects which are related to the different morphologies/sizes of the crystalline grains of phosphors.

As shown in Scheme 1, the regular $CaWO_4:Ln^{3+}$ precursor gel dots array was realized by patterning hydrophobic 1H,1H,2H,2H-perfluorooctyltrichlorosilane (PFOTS) on the substrate using a PDMS soft mold, followed by the selective deposition of the precursor solution on the hydrophilic regions by spin coating. The as-cleaned quartz substrate by piranha solution exhibited hydrophilicity with a contact angle of 9.7° (Figure 3a). In contrast, the quartz substrate modified with a monomolecular layer of PFOTS was hydrophobic with a contact angle of 102.1° (Figure 3b). Simultaneously, the PFOTS molecules were tethered onto the quartz substrate by the reaction of trichlorosilyl (Cl_3Si-) groups in

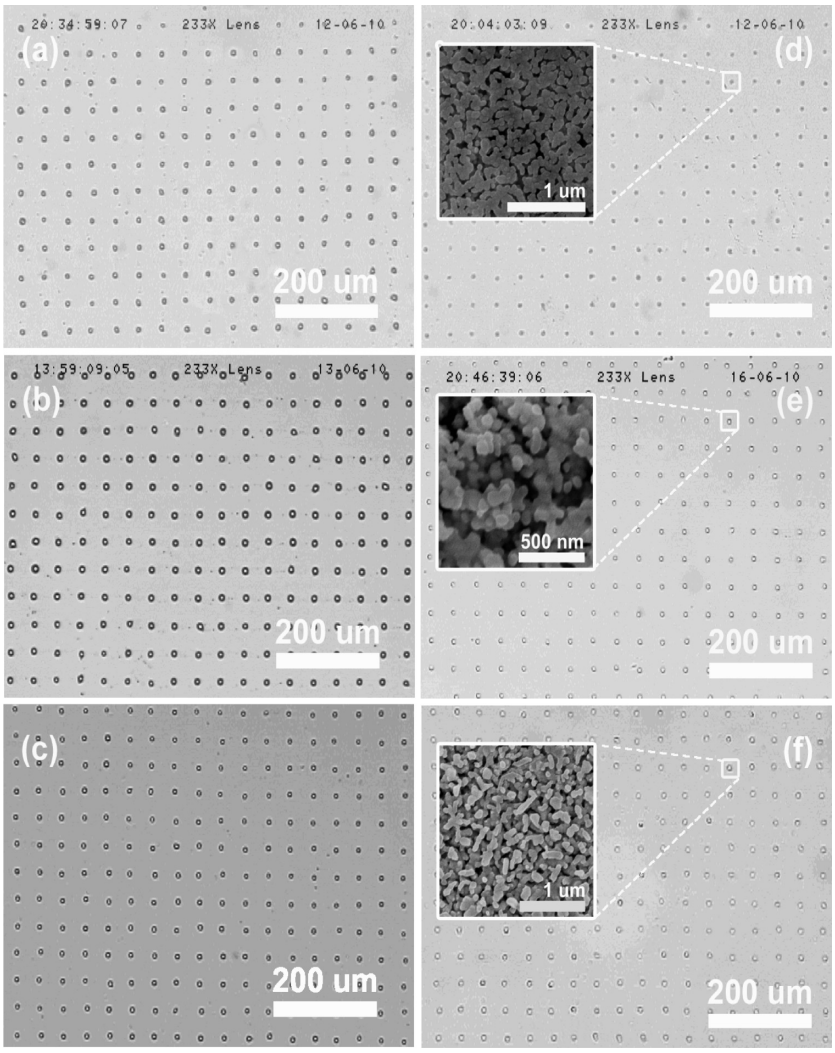

Figure 2. Optical micrographs of $CaWO_4:Eu^{3+}$ (a), $CaWO_4:Tb^{3+}$ (b), and pure $CaWO_4$ (c) precursor gel arrays, and those after heat treatment at 900 °C for $CaWO_4:Eu^{3+}$ (d), $CaWO_4:Tb^{3+}$ (e), and $CaWO_4$ (f). The insets are the SEM images of the corresponding crystalline pattern arrays.

Figure 3. Contact angles of water droplets on the piranha solution treated quartz plate (a) and after modification of a hydrophobic 1H,1H,2H,2H perfluorooctyltrichlorosilane (PFOTS) monomolecular layer on the surface (b).

PFOTS with the hydroxyl groups on the quartz substrate via the formation of a covalent siloxane (Si−O−Si) bond. Thus, the hydrophobic PFOTS molecules printed on the substrate construct a multiple microwells pattern, and the square regions within microwells are still hydrophilic.

Generally, a continuous film will start dewetting from the unfavorable hydrophobic regions, and then, the dispersed film decay into droplets and flow into the particular parts possess large affinity, which are defined by enclosing with the hydrophobic microwell fence. This process can be described as follows: first of all, the whole substrate is covered by the excess precursor solution composed of mainly hydrophilic water and ethanol. When the spin-coating process is started, the solution film becomes thinner and superfluous solution is removed. As a result, the left solution film can not spread over the entire substrate, especially on the hydrophobic region where the gravity of the film and the interface force can not balance the intermolecular force.[21] Thus, the film is ruptured at the microwell border where the chemical heterogeneity (hydrophobic against hydrophilic) is the highest, then the dewetting occurs. The volume and thickness of the film increase in the hydrophilic region under both the action of chemical potential and interface forces. However, the spreading area is constant here,

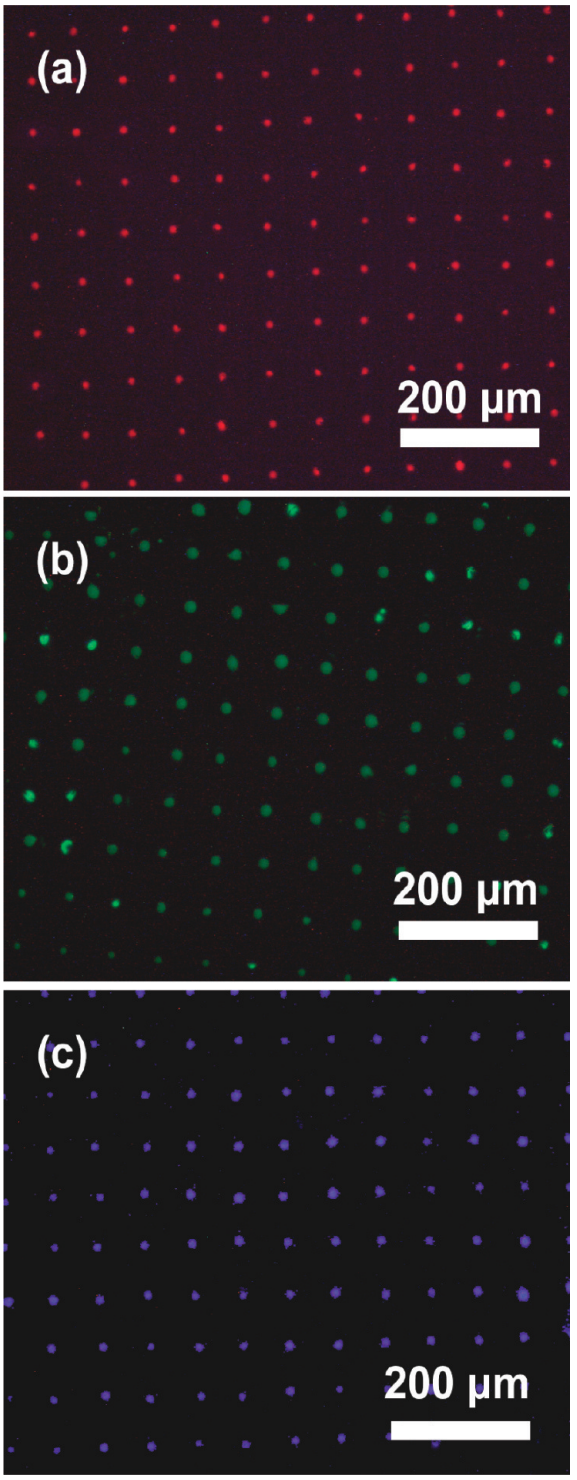

Figure 4. Fluorescence microscope images of the RGB patterns for $CaWO_4$:Eu^{3+} (a), $CaWO_4$:Tb^{3+} (b), and $CaWO_4$ (c) under 254 nm UV irradiation.

which initiates the raise of contact angle and the curvature.[22,23] Finally, the surface tension of the film increases with the curvature improvement. Meanwhile, the water and ethanol are evaporated during the high speed spin-coating process, which triggers an increase in the viscosity and the intermolecular force of the film, followed by shrinkage of the film in the hydrophilic region. Finally, the solution decays as a dot in the center of every hydrophilic square region.

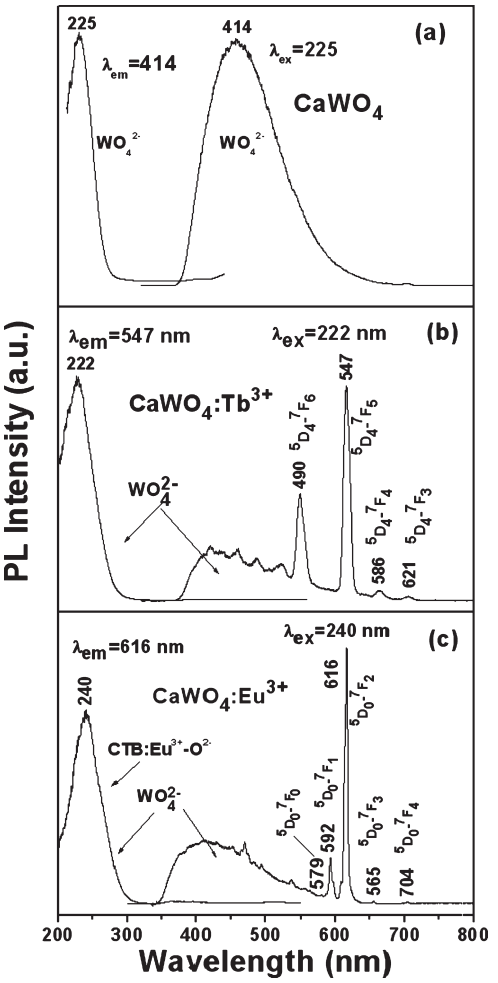

Figure 5. PL excitation and emission spectra of $CaWO_4$ (a), $CaWO_4$:Tb^{3+} (b), and $CaWO_4$:Eu^{3+} (c) patterned films.

Figure 4a–c presents the fluorescent microscope images for $CaWO_4$:Eu^{3+}, $CaWO_4$:Tb^{3+}, and $CaWO_4$ pattern film under 254 nm UV excitation, respectively. Under short wavelength ultraviolet (UV) irradiation, the as-prepared $CaWO_4$:Eu^{3+}, $CaWO_4$:Tb^{3+}, and $CaWO_4$ pattern arrays exhibit red, green, and blue luminescence, respectively. There was no light emission from other regions on the substrates, indicating that there was no superfluous or undesired gel left on the substrate after the pattern transfer process. The luminescent properties of these pattern arrays are measured by the PL spectra, as shown in Figure 5. In Figure 5a, left, the excitation spectrum of the patterned $CaWO_4$ film was obtained by monitoring the emission of WO_4^{2-} at 414 nm. An intense band from 210 to 260 nm with a maximum at 225 nm is observed, which is attributed to the charge transfer absorption from the oxygen ligands to the central tungsten atom within the WO_4^{2-} groups. In WO_4^{2-} groups, an oxygen (O) 2p electron goes into one of the empty tungsten (W) 5d orbitals to yield the excitation band. Upon excitation at 225 nm, the emission spectrum of $CaWO_4$ pattern film contains a broad band from 350 to 550 nm with a maximum at 414 nm, as shown in Figure 5a, right. From the viewpoint of molecular orbital theory, the excitation and emission bands of $CaWO_4$ can be assigned to the transitions from the $^1A_1$ ground state to the high vibration level of $^1B(^1T_2)$ and from ^1B ($^1T_2$) to the $^1A_1$ ground state within the WO_4^{2-} ion.[24]

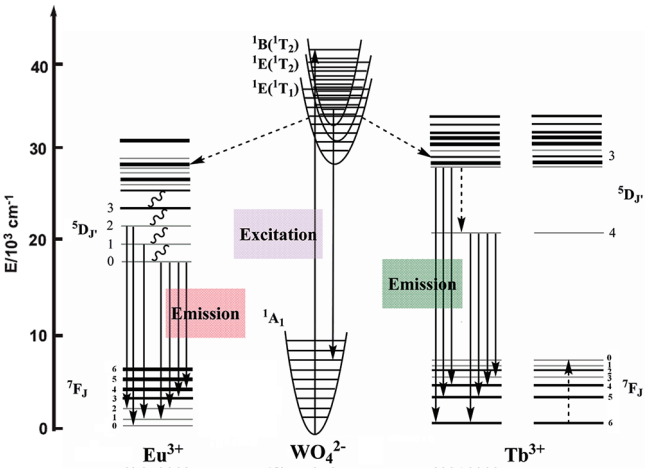

Figure 6. Energy level scheme for WO_4^{2-} groups and the energy transfer process from WO_4^{2-} to Tb^{3+} and Eu^{3+} as well as the emission process from Tb^{3+} and Eu^{3+}.

Figure 5b shows the excitation and emission spectra of the as-prepared $CaWO_4$:Tb^{3+} patterned film. The excitation spectrum (Figure 5b, left) monitored with the 547 nm emission of Tb^{3+} ($^5D_4$—$^7F_5$) consists of a band from 200 to 270 nm with a maximum at 221 nm due to the WO_4^{2-} group as described above. The presence of the absorption peak of the WO_4^{2-} group in the excitation spectrum of Tb^{3+} indicates that there is an energy transfer from WO_4^{2-} group to Tb^{3+} ions in the $CaWO_4$:Tb^{3+} luminescent pattern film.[24] Excitation into the WO_4^{2-} group at 221 nm yields the emissions spectrum corresponding to the f—f transitions of Tb^{3+}, which is dominated by the green emission of $^5D_4$—$^7F_5$ transition at 547 nm (Figure 5b, right). The emission spectrum still exhibits three other peaks centered at 490, 586, and 621 nm, originating from the characteristic $^5D_4$—^7F_J (J = 6, 4, 3) emission lines of Tb^{3+}. Compared with the emission peaks of Tb^{3+}, the intrinsic blue emission from WO_4^{2-} groups is weaker, suggesting that an efficient energy transfer from WO_4^{2-} groups to Tb^{3+} has occurred. Furthermore, the emission from the $^5D_3$ level of Tb^{3+} is much weaker than that from the $^5D_4$ level due to the cross relaxation effect of Tb^{3+}. $CaWO_4$ phosphor crystallizes in a tetragonal scheelite structure with a space group of C_{4h}, in which the Ca^{2+} ion is coordinated by eight oxygen atoms and has S_4 point symmetry.[25] The similarity of ionic radius between Tb^{3+} (0.92 Å) and Ca^{2+} (1.12 Å) makes the substitution of Tb $^{3+}$ for the Ca^{2+} ion occur.[26] Considering the different oxidation states of Tb^{3+} and Ca^{2+}, the actual site symmetry of Tb^{3+} might deviate from S_4 due to the charge compensating effects. Ghaderi and co-workers described the charge compensating pattern as $3Ca^{2+} \rightarrow 2Tb^{3+} + \square$, where the $\square$ is a Ca^{2+} site vacancy.[27] The similar situation holds for $CaWO_4$:Eu^{3+}, i.e., $3Ca^{2+} \rightarrow 2Eu^{3+} + \square$. The presence of the very weak Eu^{3+} $^5D_0$—$^7F_0$ emission (579 nm in Figure 5c), which is only allowed for C_s, C_n, and C_{nv} site symmetry,[28] can confirm the deviation of Eu^{3+} in the contorted lattice and the effect on the luminescent properties.

A summary of the emission and energy transfer process in $CaWO_4$:Tb^{3+} is shown schematically in Figure 6. Upon UV (220 nm) excitation, an electron in the ground state ($^1A_1$) is excited into the ^1B ($^1T_2$) level of WO_4^{2-}, where either the electron relaxes to its lowest excited ^1B ($^1T_2$) level of WO_4^{2-}, producing the emission by the transition to the $^1A_1$ level, or the excitation energy transfers to Tb^{3+} $^5D_3$ or higher levels by a

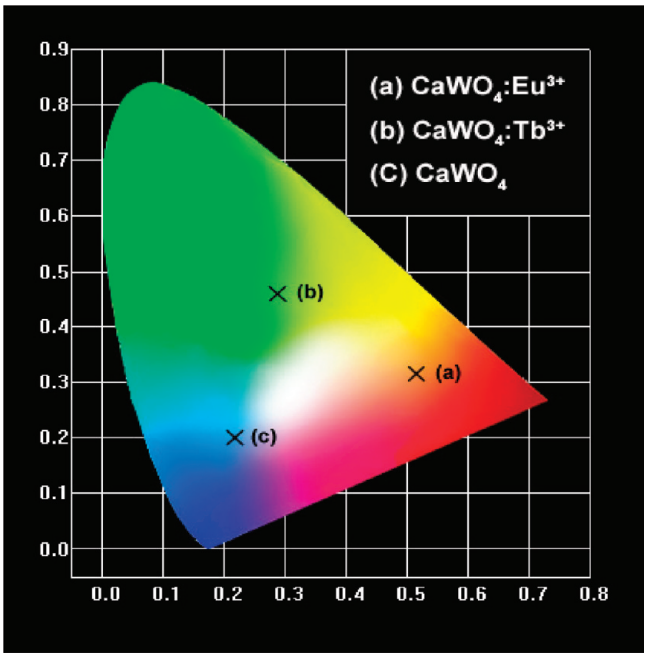

Figure 7. CIE chromaticity diagram of luminescent $CaWO_4$:Eu^{3+} (point a), $CaWO_4$:Tb^{3+} (point b), and $CaWO_4$ (point c) patterns.

resonance process. The relaxation from $^5D_3$ to $^5D_4$ cannot happen by a multiphonon relaxation process due to the large energy difference between these two levels in the range of 5700 cm^{-1}.[29] By an alternative way, the energy was effectively transferred to the $^5D_4$ energy level of the adjacent Tb^{3+} through a cross relaxation process. This should be ascribed to a high concentration of Tb^{3+} (5%) as well as the energy difference between the $^5D_3$ and $^5D_4$ excited states, matching approximately the energy difference between the $^7F_6$ ground state and higher ^7F_J states of Tb^{3+}.[30] Therefore, the cross relaxation quenched the emission from the $^5D_3$ level and greatly enhanced the emission originating from the $^5D_4$ level to ground states of Tb^{3+}, resulting in the dominant green light emission.

Figure 5c gives the excitation and emission spectra of the patterned $CaWO_4$:Eu^{3+} film. The excitation spectrum (left) mainly consists of a broad band with a maximum at 240 nm monitored by the $^5D_0$—$^7F_2$ transition of Eu^{3+} at 616 nm, which shows a red shift with respect to the absorption of $CaWO_4$ host lattice (221 nm) due to the contribution of the charge transfer transition of Eu^{3+}—O^{2-} besides the WO_4^{2-}. Some tiny waves in the longer-wavelength region should arise from the f—f transitions within the Eu^{3+} $4f^6$ electron configuration. Their extremely weak intensities can be attributed to the forbidden nature of f—f transitions, which have much smaller absorption area and oscillator strength with respect to the WO_4^{2-} and Eu^{3+}—O^{2-} charge transfer band. Upon excitation at 240 nm, the emission spectrum (Figure 5c, right) of $CaWO_4$:Eu^{3+} contains not only a weak emission belong to the WO_4^{2-} group from 350 to 600 nm but also a series of resolved features at 592, 616, 665, and 704 nm, which correspond to the $^5D_0$—^7F_J (J = 1, 2, 3, 4) transition of Eu^{3+}. Among them, the hypersensitive $^5D_0$—$^7F_2$ (616 nm) red emission is the most prominent. Similarly, the presented emissions of Eu^{3+} by excitation of WO_4^{2-} group should be ascribed to the energy transfer from the WO_4^{2-} to the Eu^{3+} ions. The locations of the emission lines of Eu^{3+} and their assignments are indicated

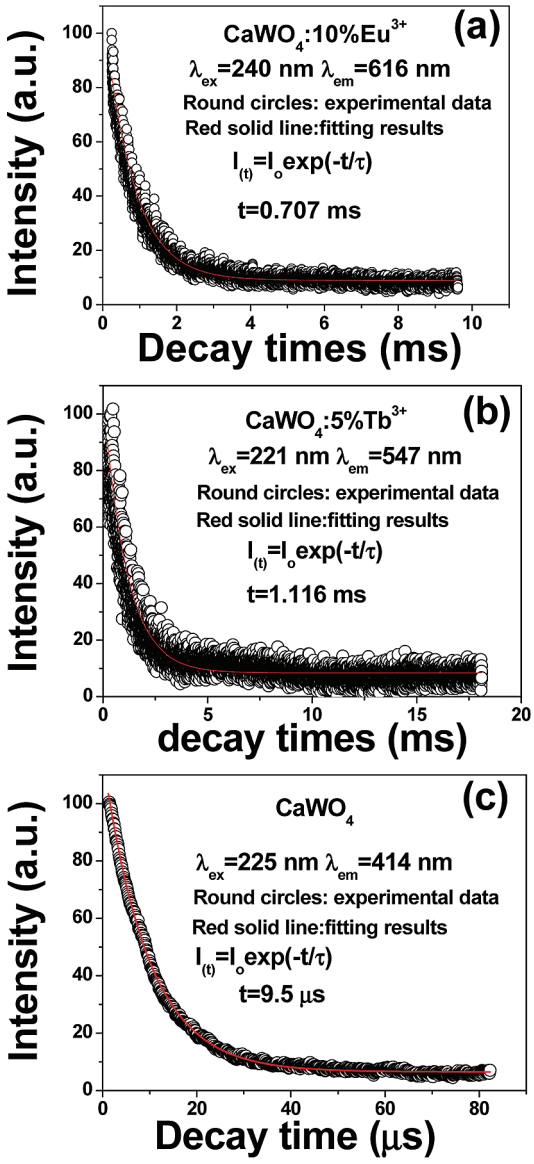

Figure 8. Decay curves for the luminescence Eu^{3+} ($^5D_0-^7F_2$ at 616 nm, a), Tb^{3+} ($^5D_4-^7F_5$ at 547 nm, b), and WO_4^{2-} (414 nm, c) in the patterned crystalline $CaWO_4$ films.

in Figure 5c, and the corresponding energy transfer process is shown in Figure 6. The excitation energy transfers from ^1B ($^1T_2$) level of WO_4^{2-} group to Eu^{3+} $^5D_3$ or higher levels by a resonance process, from which the energy nonradiatively relaxes to the $^5D_0$ level by multiphonon relaxation. Then, the characteristic emissions of $^5D_0-^7F_J$ (J = 0, 1, 2, 3, 4) of Eu^{3+} occur, which demonstrates a strong red color emission.

The chromaticity coordinates (CIE) of these RGB patterned films are presented in Figure 7. The coordinates of (a) x = 0.516 and y = 0.316, (b) x = 0.287 and y = 0.461, and (c) x = 0.217 and y = 0.200 are corresponding to $CaWO_4$:Eu^{3+}, $CaWO_4$:Tb^{3+}, and undoped $CaWO_4$ crystal films, indicating the emissions in the red, green, and blue region, respectively. Here, the demo shows that the multicolor emissions can be realized by a single UV or e-beam excitations within $CaWO_4$:Ln^{3+} series compounds, which is beneficial for the potential device fabrication. However, it still has a long way to achieve the standard of National Television System Committee (NTSC) for a practical color display device since their smaller area of color gamut is revealed in the chromaticity diagram. In addition, fabrication of a color device needs patterning RGB subpixels arrays on the same substrate, and they compromise in the generation of white light by adjusting the intensities of each subpixel. However, under the current stage, there are still many difficulties and challenges for realization of color pixels array only by soft lithographic methods, but the beneficial attempts in this study provided the possibilities for fabricating single-color device and the potential manufacture strategies for color device by combing with the other patterning methods such as inkjet printing and electrophoretic deposition.

The PL decay curves of Eu^{3+} in $CaWO_4$:Eu^{3+}, Tb^{3+} in $CaWO_4$:Tb^{3+}, and WO_4^{2-} in $CaWO_4$ are shown in Figure 8a–c, respectively. These curves can be well fitted by a single exponential function as $I(t) = I_0\exp(-t/\tau)$ where I_0 is the initial emission intensity at $t = 0$ and τ is the 1/e lifetime of the emission center. The formula indicates that all the Eu^{3+} or Tb^{3+} occupy the same coordination environment, and the luminescence lifetimes of Eu^{3+} and Tb^{3+} can be determined to be 0.767 and 1.067 ms, respectively. The luminescence liftime of WO_4^{2-} in $CaWO_4$ is 9.5 μs, which is much shorter than those of Eu^{3+} (0.767 ms) and Tb^{3+} (1.067 ms) and enable the energy transfer process from WO_4^{2-} to the doped ions. These results were well in agreement with the previous studies for the lifetimes of the lanthanide-doped $CaWO_4$.[23,31]

4. CONCLUSION

We have demonstrated the realization of multicolor luminescent patterning films of $CaWO_4$:Ln^{3+} (Ln = Eu, Tb) and $CaWO_4$ on quartz substrates by the microcontact printing method combining with the Pechini sol–gel route. The regular dot arrays of $CaWO_4$: Eu^{3+}, $CaWO_4$:Tb^{3+}, and $CaWO_4$ films emit red, green, and blue (RGB) luminescence upon UV-light irradiation, respectively. This facile and straightforward method may be extended to prepare various other phosphor patterns, thus opening ways to fabricate light-emitting pixels for display device applications via a soft-lithography process.

AUTHOR INFORMATION

Corresponding Author

*E-mail: jlin@ciac.jl.cn (J.L.); zycheng@ciac.jl.cn (Z.C.).

ACKNOWLEDGMENT

This project is financially supported by the National Natural Science Foundation of China (NSFC 60977013, 50872131, 20921002) and the National Basic Research Program of China (2007CB935502, 2010CB327704).

REFERENCES

(1) Muller, C. D.; Falcou, A.; Reckefuss, N.; Rojahn, M.; Wiederhirn, V.; Rudati, P.; Frohne, H.; Nuyken, O.; Becker, H.; Meerholz, K. *Nature* **2003**, *421*, 829–833.

(2) Ninjbadgar, T.; Garnweitner, G.; Borger, A.; Goldenberg, L. M.; Sakhno, O. V.; Stumpe, J. *Adv. Funct. Mater.* **2009**, *19*, 1819–1825.

(3) Carlos, L. D.; Ferreira, R. A. S.; Bermudez, V. D.; Ribeiro, S. J. L. *Adv. Mater.* **2009**, *21*, 509–534.

(4) Ying, G. Y.; Hu, W. B.; Qiu, Y. In *The Technology of Flat Panel Displays*; Fu, J., Ed.; Post & Telecom Press: Bejing, China, 2002.

(5) Cavallini, M.; Albonetti, C.; Biscarini, F. *Adv. Mater.* **2009**, *21*, 1043–1053.
(6) Cheng, Z.; Xing, R.; Hou, Z.; Huang, S.; Lin, J. *J. Phys. Chem. C* **2010**, *114*, 9883–9888.
(7) Xia, Y. N.; Whitesides, G. M. *Angew. Chem., Int. Ed.* **1998**, *37*, 551–575.
(8) (a) Lahiri, J.; Ostuni, E.; Whitesides, G. M. *Langmuir* **1999**, *15*, 2055–2060. (b) Smith, R. K.; Lewis, P. A.; Weiss, P. S. *Prog. Surf. Sci.* **2004**, *75*, 1–68. (c) Wang, W.; Cheng, Z.; Yang, P.; Hou, Z.; Li, C.; Li, G.; Dai, Y.; Lin, J. *Adv. Funct. Mater.* **2010**, *21*, 456–463.
(9) Ozbay, E.; Michel, E.; Tuttle, G.; Biswas, R.; Sigalas, M.; Ho, K. M. *Appl. Phys. Lett.* **1994**, *64*, 2059–2061.
(10) Li, G.; Hou, Z.; Peng, C.; Wang, W.; Cheng, Z.; Li, C.; Lian, H.; Lin, J. *Adv. Funct. Mater.* **2010**, *20*, 3446–3456.
(11) Tanner, P. A.; Yan, B.; Zhang, H. J. *J. Mater. Sci.* **2000**, *35*, 4325–4328.
(12) Li, G. G.; Li, C. X.; Zhang, C. M.; Cheng, Z. Y.; Quan, Z. W.; Peng, C.; Lin, J. *J. Mater. Chem.* **2009**, *19*, 8936–8943.
(13) Carlos, L. D.; Messaddeq, Y.; Brito, H. F.; Ferreira, R. A. S.; Bermudez, V. D.; Ribeiro, S. J. L. *Adv. Mater.* **2000**, *12*, 594–598.
(14) Tang, Y. S.; Hu, S. F.; Lin, C. C.; Bagkar, N. C.; Liu, R. S. *Appl. Phys. Lett.* **2007**, *90*, 151108.
(15) Cushing, B. L.; Kolesnichenko, V. L.; O'Connor, C. J. *Chem. Rev.* **2004**, *104*, 3893–3946.
(16) Higashi, K.; Sonoda, K.; Ono, H.; Sameshima, S.; Hirata, Y. *J. Mater. Res.* **1999**, *14*, 957–968.
(17) Lin, J.; Yu, M.; Lin, C. K.; Liu, X. M. *J. Phys. Chem. C* **2007**, *111*, 5835–5845.
(18) Hou, Z. Y.; Chai, R. T.; Zhang, M. L.; Zhang, C. M.; Chong, P.; Xu, Z. H.; Li, G. G.; Lin, J. *Langmuir* **2009**, *25*, 12340–12348.
(19) (a) Maurera, M. A.; Souza, A. G.; Soledade, L. E. B.; Pontes, F. M.; Longo, E.; Leite, E. R.; Varela, J. A. *Mater. Lett.* **2004**, *58*, 727–732. (b) Saito, N.; Sonoyama, N.; Sakata, T. *Bull. Chem. Soc. Jpn.* **1996**, *69*, 2191–2194.
(20) Yu, M.; Lin, J.; Wang, Z.; Fu, J.; Wang, S.; Zhang, H. J.; Han, Y. C. *Chem. Mater.* **2002**, *14*, 2224–2231.
(21) Wyart, F. B.; Martin, P.; Redon, C. *Langmuir* **1993**, *9*, 3682–3690.
(22) Xue, L. J.; Gao, X.; Zhao, K.; Liu, J. G.; Yu, X. H.; Han, Y. C. *Nanotechnology* **2010**, *21*, 145303 (9 pages).
(23) Xue, L. J.; Han, Y. C. *Langmuir* **2009**, *25*, 5135–5140.
(24) Jia, P. Y.; Liu, X. M.; Li, G. Z.; Yu, M.; Fang, J.; Lin, J. *Nanotechnology* **2006**, *17*, 734–742.
(25) Page, A. G.; Godbole, S. V.; Sastry, M. D. *J. Phys. Chem. Solids* **1989**, *50*, 571–575.
(26) Lu, Z. G.; Chen, L. M.; T ang, Y. G.; Li, Y. D. *J. Alloys Compd.* **2005**, *387*, L1–L4.
(27) Ghaderi, M.; Palin, J. M.; Campbell, I. H.; Sylvester, P. J. *Econ. Geol. Bull. Soc.* **1999**, *94*, 423–437.
(28) Blasse, G.; Bril, A. *Philips Res. Rep.* **1966**, *2*, 368.
(29) Blasse, G.; Grabmaier, B. C. *Lnminescent Materials*; Spinger-Verlag: Berlin Heidelberg, 1994.
(30) (a) Ronda, C. *Luminescence, From Theory to Applications*; WILEY-VCH Verlag GmbH & Co. KGaA: Weinheim, 2008. (b) Lei, F; Yan, B. *J. Solid State Chem.* **2008**, *181*, 855–862.
(31) (a) Su, Y. G.; Li, L. P.; Li, G. S. *J. Mater. Chem.* **2009**, *19*, 2316–2322. (b) Pang, M. L; Lin, J.; Wang, S. B.; Yu, M.; Zhou, Y. H.; Han, X. M. *J. Phys.: Condens. Matter* **2003**, *15*, 5157–5169. (c) Su, Y. G.; Li, L. P.; Li, G. S. *Chem. Mater.* **2008**, *20*, 6060–6067. (d) Bourcet, J. C.; Fong, F. K. *J. Chem. Phys.* **1974**, *60*, 34–39.